# 2. Experimental studies on disordered NbN thin films

Now, what do you own the world?
How do you own disorder, disorder?
Somewhere between the sacred silence and sleep
Disorder, disorder, disorder

*System of a Down*

*Content of this chapter are optical studies on NbN thin films on approach of the superconductor-insulator quantum phase transition (SIT) providing experimental evidence for the existence of the Higgs mode. We will start our discussion in Sec. 2.1 with some theoretical considerations regarding superconductivity and disorder followed by a review of hallmark tunneling-spectroscopy studies on homogeneously disordered SIT materials in Sec. 2.2. Subsequently in Sec. 2.3, we will discuss measurements of the dynamical conductivity of a series of NbN films covering the range from clean to strongly disordered and compare the results with measurements of the (differential) tunneling conductance. We will see that the mutual analysis within a model inspired by the paramagnetic pair-breaking theory of Abrikosov and Gor'kov reveals a discrepancy between both spectroscopies that cannot be explained by pair-breaking effects only but rather calls for for radically new ideas. Given the specific nature of short coherence-length quasi-2d NbN near quantum criticality we will in Sec. 2.4 present an explanation involving an excitation of the superconducting order parameter namely the Higgs mode - a condensed-matter realization of what is best known as Higgs boson in particle physics yet sharing the same origin: spontaneous symmetry breaking. We will discuss experimental results justifying this interpretation, yet also open questions concerning the visibility of the Higgs mode in disordered systems, Sec. 2.5.*



U. S. Pracht, *Electrodynamics of Quantum-Critical Conductors and Superconductors*, Springer Theses,
https://doi.org/10.1007/978-3-319-72802-5_2

## 2.1 The superconductor-insulator quantum phase transition

A prototypical quantum phase transition in condensed matter is the transition between superconducting and insulating ground states of an electronic system at zero temperature in two spatial dimensions (2d). This superconductor - insulator transition (SIT) can be tuned by various parameters, most importantly lattice impurities acting as source for weak localization effects or potential traps strongly localizing charge carriers. The special appeal of the SIT and associated phenomena lies in its intermediate position framed by two of the most fundamental paradigms of condensed matter physics, namely the Anderson theorem for superconductivity and the Anderson localization each of which breaks down at the SIT giving rise to intriguing physics vivified by the interplay of localization and condensation. In what follows, we will briefly examine both paradigms and qualitatively introduce the two fundamental scenarios possibly leading to the cease of superconductivity at the quantum critical point[39].

[39] For an comprehensive review of this topic the interested reader is referred to the reviews of Gantmakher and Dolgopolov [14] and Lin, Nelson and Goldman [15]. Also, the textbook by Dobrosavljevic, Trivedi, and Valles [16] provides a valuable collection of articles introducing theoretical approaches and experimental hallmarks.

### 2.1.1 The insulating side: scaling theory of conductivity

Maybe the most stunning aspect of the SIT in 2d lies in the direct transition between two ground states, which could not be any more different. On the one side, a coherent many-body ground state composed of delocalized Cooper pairs (a superconductor) and, on the other side, a ground state with incoherent and localized quasiparticles (an insulator) presumably *without* an intermediate ground state of incoherent but delocalized quasiparticle states (a metal). To understand the absence of this intermediate metallic state one can employ the *single parameter scaling* argument [17] suggested by Abrahams, Anderson, Licciardello, and Ramakrishnan[40] which is an elegant application of the renormalization-group ideas: Start with a cube of spatial dimension $d = 1, 2, 3$ and side lengths $L$, then find expressions for the conductance, define a scaling function thereof and study the general implications by sending $L \to \infty$. For a metal in the

[40] also known as the *gang of four*

high-conductivity ($\sigma$) limit the conductance $g$ is simply

$$g_m = \sigma L^{d-2} \tag{2.1}$$

which is easily verified for the dimensions above. For insulators in the low-conductivity localization limit, one can expect a conductance which is exponentially damped on a characteristic length scale $\xi$

$$g_i = g_c e^{-L/\xi}. \tag{2.2}$$

While at intermediate regimes the particular form of $g$ surely depends on details of electron transport and incipient localization, we will see that the asymptotic limits Eqs. (2.1) and (2.2) are sufficient to understand the essential physics. For a renormalization treatment removing the explicit dependence on $L$, Abrahams *et al.* suggested the scaling function

$$\beta(g) \equiv \frac{\mathrm{d}\ \ln g}{\mathrm{d}\ln L}. \tag{2.3}$$

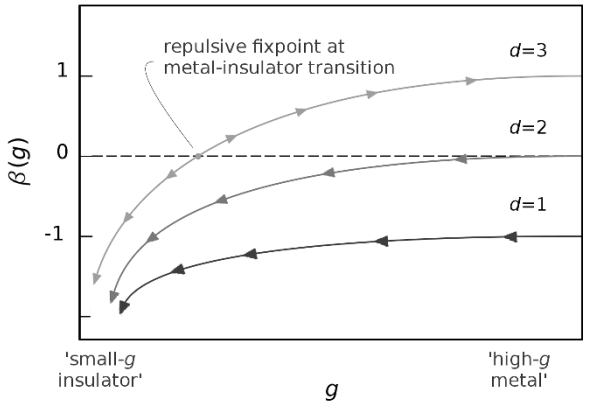


*Figure 2.1: single-parameter-scaling function $\beta$ of a $d$-dimensional cube $L^d$ versus conductance interpolating between logarithmic decay (insulating limit) and saturation (metallic limit) in 1,2, and 3 spatial dimensions. Arrows indicate the renormalization flow in the limit $L \to \infty$. For $d = 1$ and 2 any amount of disorder will always favor the insulating ground state over the metallic one, whereas for $d = 3$ the system has a metal-to-insulator transition at an repulsive fix point.*

Inserting the explicit expressions Eq. (2.1,2.2) gives the limits

$$\lim_{g\to\infty} \beta(g) = d-2, \tag{2.4}$$

$$\lim_{g\to 0} \beta(g) = \ln\left(\frac{g(L)}{g_c}\right). \tag{2.5}$$

Figure 2.1 displays schematically $\beta(g)$ for $d$ =1,2, and 3 dimensions. In the insulating limit, all curves collapse irrespective of dimensionality, while in the metallic limit, the asymptotes are different and only the 3d case features a zero-crossing at a critical conductance $g_c$. Now we consider the *renormalization flow* upon coarse graining, indicated by the arrows in Fig. 2.1. For small disorder, we will obtain a conductance $g_0 > g_c$, and sending $L \to \infty$ for $d = 3$ will increase the conductance as $g = \sigma L$ pushing the system towards the metallic limit, whereas for $g_0 < g_c$ at high disorder the conductance will rather decrease dragging the system towards to insulating regime. The system is said to *flow* away from the repulsive fix point at $g_c$ either towards metallic or insulating ground states depending on the specific disorder. This is the so-called metal-to-insulator quantum phase transition (MIT) at the mobility edge $g_c$ purely driven by disorder. In $d = 1$ and 2 the situation is distinctly different. Here, increasing $L$ will leave the conductance unaffected $g = \sigma$ ($d = 2$) or reduce it as $g = \sigma/L$ ($d = 1$). The drag towards the insulator cannot be compensated by an attractive metallic limit so that even the smallest amount of disorder will unavoidably cause a flow towards the insulating ground state. In other words, in dimensions $d < 3$ *no* metallic ground state is possible at $T = 0$. Note that the above reasoning does not rely on specific details of $g(L)$. It can be shown, that quantum corrections to transport will affect the specific functional forms, but there is *never* a mobility edge in less than 3 spatial dimensions [17].

### 2.1.2 The superconducting side: Anderson theorem

Although superconductivity as ground state of electronic systems is limited to comparably low energy scales $T_c \sim 10\,\mathrm{K}$, its ubiquitous appearance as favorable ground state

of numerous materials ranging from single crystals to amorphous films results from its insensitivity against disorder. While the above scaling arguments rules out a 2d metal, this insensitivity can qualitatively be seen as reason for 2d superconductors - a celebrated result first obtained by Anderson [18] and commonly referred to as Anderson theorem. A comprehensive discussion of the Anderson theorem is lengthy and beyond the scope of this work. Instead, we will only sketch the succession of arguments leading to the conclusion[41].

The electron-phonon interaction term $H$ of the BCS Hamiltonian $H_0$ for clean superconductors reads[42]

$$H = V \sum_{\mathbf{k}} \hat{c}^\dagger_{\mathbf{k}\uparrow} \hat{c}^\dagger_{-\mathbf{k}\downarrow} \hat{c}_{-\mathbf{k}'\downarrow} \hat{c}_{\mathbf{k}'\uparrow} \tag{2.6}$$

pairing states with opposite momenta and spin, i.e. $(\mathbf{k}, \uparrow)$ and $(-\mathbf{k}, \downarrow)$. The BCS mean-field approximation diagonalizes this Hamiltonian and leads to the well-known energy spectrum $E_{\mathbf{k}} = \sqrt{(\epsilon_{\mathbf{k}} - \mu)^2 + |\Delta|^2}$ with $\epsilon_{\mathbf{k}}$ and $\mu$ the band dispersion and chemical potential and the BCS self-consistency equation

$$\Delta = VN(0) \int d\xi \frac{\Delta}{2\sqrt{(\xi - \mu)^2 + |\Delta|^2}}. \tag{2.7}$$

In disordered systems, the lattice translational symmetry is lifted and scattering off impurities violates conservation of momentum such that $\mathbf{k}$ is no longer a good quantum number and Cooper pairs do no longer result from the above pairing scheme. Anderson showed, that the BCS condition for pairing can be generalized beyond $|\mathbf{k}, \uparrow\rangle$ and $|-\mathbf{k}, \downarrow\rangle$ to exact eigenstates $|\alpha\rangle$ of the disordered Hamiltonian $H'$ and their time-reversed counterparts $\hat{T}|\alpha\rangle$ yet restoring the energy spectrum and self-consistency equation above. Starting point is the general electron-phonon interaction operator

$$H = V \sum_{\mathbf{k},\mathbf{k}',\mathbf{q}} \sum_{\sigma,\sigma'} \hat{c}^\dagger_{\mathbf{k}'+\mathbf{q},\sigma'} \hat{c}^\dagger_{\mathbf{k}-\mathbf{q},\sigma} \hat{c}_{\mathbf{k},\sigma} \hat{c}_{\mathbf{k}',\sigma'}. \tag{2.8}$$

Transformation[43] of the $\mathbf{k}$-space operators to real-space operators $\hat{\psi}(\mathbf{r})$, subsequent integration, and spin sum-

[41] What follows is based on the more comprehensive discussion in Ref. [19].

[42] with the usual notion of fermionic creation and annihilation operators $\hat{c}^\dagger, \hat{c}$ and a constant interaction potential $V$

[43] via the Fourier integral

$$\hat{c}_{\mathbf{k},\sigma} = \int d\mathbf{r} \hat{\psi}(\mathbf{r}) e^{i\mathbf{kr}}$$

mation yields

$$H = 2V \int d\mathbf{r} \hat{\psi}^\dagger_\uparrow(\mathbf{r}) \hat{\psi}^\dagger_\downarrow(\mathbf{r}) \hat{\psi}_\downarrow(\mathbf{r}) \hat{\psi}_\uparrow(\mathbf{r}). \qquad (2.9)$$

In general, the orbitals $\hat{\psi}(\mathbf{r})$ will be complicated functions of $\mathbf{r}$ for a randomly disordered lattice. For the sake of the argument, however, the actual form is not required given the *existence* of a set of eigenstates $|\alpha\rangle$ (and corresponding orbitals $\hat{\phi}_\alpha(\mathbf{r})$) diagonalizing the Hamiltonian for the disordered problem. Transformation into this new basis[44], the Hamiltonian Eq. (2.9) can be cast into the BCS mean-field form with the only difference that the operators create and annihilate (time-reversed) eigenstates $|\alpha\rangle$ instead of momentum eigenstates $|\mathbf{k}\rangle$. After diagonalization and Bogoliubov transformation[45] one finds a similar spectrum $E_\alpha = \sqrt{(\epsilon_\alpha - \mu)^2 + |\Delta|^2}$ which still contains information about the specific choice of eigenstates in terms of the eigenvalues $\epsilon_\alpha$. To obtain the self-consistency equation, however, any reference to the basis is lost when the summation over eigenvalues $\epsilon_\alpha$ is replaced by an continuous integral so that the BCS result Eq. (2.7) is exactly restored. Consequently, disorder has no impact on the superconducting properties. In other words, if impurity scattering were to destroy a Cooper pair it would need to lift the requirement of time-reversal symmetry. Scattering off an potential, however, preserves the spin orientation and hence no pair-braking takes place, *as long as* the scatterer does not carry a magnetic moment: in this case, time-reversal symmetry is broken and superconductivity may be strongly suppressed [20, 21, 22].

[44] via the spectral representation

$$\hat{\psi}_\sigma(\mathbf{r}) = \sum_\alpha \hat{\phi}_\alpha(\mathbf{r}) \hat{c}_{\alpha,\sigma}$$

[45] that is, introducing new fermionic operators creating and annihilating quasiparticles (instead of electrons) which allow to transform the complicated 4-operator term in Eq. (2.8) into a harmonic oscillator.

### 2.1.3 The quantum-critical regime

The Anderson theorem and the Anderson localization sketched above determine the physics far from the SIT at moderate and extreme amounts of disorder, respectively. As both asymptotic regimes are continuously connected, there must be a regime of disorder, where both paradigms break down and where, pictorially speaking, electrons cannot decide whether to pair up and condense or to get localized.

How can we escape Anderson's theorem? The important assumption Anderson made was that the orbitals $\hat{\phi}_\alpha(\mathbf{r})$

of the disordered system are extended in space. Only then the mean-field approximation in accordance with BCS works. Clearly, spatial extension and localization tendencies antagonize compromising the prerequisites of Anderson's theorem. An important measure to put a number on disorder is the Ioffe-Regel parameter $k_F\ell$, i.e. the product of the Fermi wave vector $k_F$ and the electron mean free path $\ell$. For marginal disorder, $k_F\ell \gg 1$ and the Anderson theorem holds, while for extreme disorder[46] $k_F\ell \approx 1$ and the system turns insulating signaling the ultimate break down of Anderson's theorem. While this explains the conceptual demand for an SIT, it does not provide an answer to the question how superconductivity actually ceases. Over the past years, two models have been put forward by theory, the so-called fermionic and the bosonic scenarios we will now briefly discuss.

[46] In this case, electrons scatter from *each* lattice site, i.e. the mean free path is the lattice constant.

### The amplitude-driven or fermionic SIT

In a seminal work [23] Finkelstein has shown that disorder tends to renormalize Coulomb interaction between electrons such that the screening becomes less efficient: the attractive Cooper interaction pairing up electrons is challenged by the repulsive Coulomb interacting lowering the energy gain upon condensation. At a critical disorder, Coulomb repulsion is strong enough to overcompensate the pairing interaction and the bound state is no longer favorable. Using a diagrammatic renormalization approach, Finkelstein demonstrated that the amplitude of the order parameter vanishes uniformly at the SIT yet. At the same time, also the superfluid density and -stiffness go to zero where the latter always remains the greater energy scale, see Fig. 2.2. The insulating side contains fermionic quasiparticles which in 2d immediately localize forming a hard insulator whereas in 3d tend the insulating behavior may be weaker according to the scaling of conductivity discussed above. The fermionic scenario has been successfully applied to explain the suppression of $T_c$ in homogeneously disordered ultra-thin films of, e.g., amorphous MoGe [24] or polycrystalline TiN [25] and MoC [26, 27]. At the same time - and not unsurprisingly - it fails to properly describe experimental results in the very vicinity of the SIT as it neglects quantum fluctuations relevant at low energies.

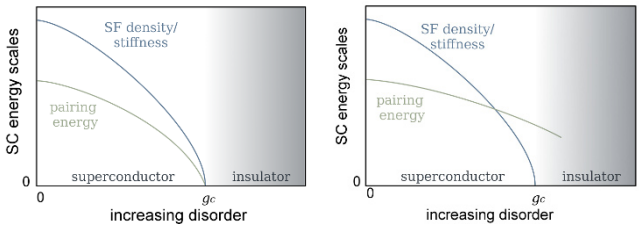


*Figure 2.2:* ***Energy scales at the SIT*** *within the fermionic (left) and the bosonic (right) scenario for the SIT. In the first case, pairing amplitude and superfluid density (or stiffness) go to zero at the QCP for critical disorder $g_c$ and the insulator contains localized fermions. In the bosonic scenario, the SIT is marked by a loss of superfluid coherence while pairing remains robust into the Cooper-pair (or Bose-) insulator.*

### The phase-driven or bosonic SIT

In the bosonic scenario global coherence necessary to form a phase-locked macroscopic superfluid condensate is lost at the SIT, see Fig. 2.2. In more detail, Fisher *et al.* have shown in a pioneering work [28] that long-range phase fluctuations among a charged ($2e$) bosonic superfluid are enhanced in approach of the SIT reducing the superfluid stiffness and finally destroying superconductivity. As a natural consequence, the bosonic model allows pairs to survive into the insulating side, where they, however, have lost a global phase coherence and become localized. This model features an intriguing charge-vortex duality which predicts a universal resistance $R_c = h/4e^2$ right at the SIT. Indeed, early dc-transport studies [29] of ultra-thin $a-$Bi films quench condensed on Ge reveal a SIT at the predicted universal resistance. Later on the prediction was found at odds with other systems, e.g. ultra-thin MoGe films: Although magneto-transport measurements confirmed the localization trend of Cooper pairs at the field-induced SIT, the importance of phase fluctuations and long-range Coulomb interaction [30], the obtained critical resistance seems sample-dependent and is scattered widely around $h/4e^2$. The discrepancy is commonly attributed to the missing fermionic degrees of freedom which naturally arises treating the Cooper pairs as hard-core charge-$2e$

bosons without internal fermionic structure.
The limited applicability of both models calls for a unified *amplitude-phase* theory equally capturing Coulomb interactions and phase fluctuations each of which are the central aspects of the respective models. At the time of writing this thesis, such a theory is yet to be developed.

In the next section we will discuss some of the hallmark experiments elucidating the SIT to conceptually outline what a successful theoretical treatment would have to account for.

## 2.2 Tunneling spectroscopies on the SIT

We will restrict our discussion to SIT systems relevant for the scope of this thesis, namely TiN and NbN. These materials can be produced in various ways as thin film with a homogeneous amorphous or polycrystalline structure and random distribution of atomic-scale disorder. The distance to the SIT can be tuned either by composition (i.e. varying $N$ concentration) or thickness. The arguably most striking result was obtained by measurements of the local tunneling conductance. Far from criticality, the energy gap $\Delta$ is uniform in space as expected for ordinary $s$-wave superconductors. This changes drastically in approach of the SIT where - despite structural homogeneity - measurements reveal a strongly inhomogeneous superconducting state. For TiN, Sacepe *et al.* resolved a spatially fluctuating energy gap $\Delta$ [25] while for NbN inhomogeneities are identified by variations of the coherence-peak height and zero-bias anomalies [31]. In both cases, the emergent superconducting domains exist on length scales comparable to a few times the superconducting coherence length of $\sim 10$ nm, i.e. much larger than the atomic-scale disorder potential traps. The emergent electronic inhomogeneity tends to localize the Cooper pairs into weakly coupled superconducting puddles. The global superconducting phase, which, in the clean case, acquires its lock to a constant value by virtue of perfect delocalization, is subject to increasingly strong fluctuations, as decomposition into weakly coupled puddles increases. The long-range phase

coherence is eventually destroyed when the charging energy[47] of the puddles by far exceeds the Josephson energy[48]. This peculiar inhomogeneity of the superconducting state is in perfect agreement with calculations within the Bogoliubov de-Gennes model [32, 33] and favors the bosonic scenario of the SIT. This view is strengthened by tracing the energy towards the SIT. Comparison of $T_c$ and tunneling gap $\Delta$ revealed a less strong decay of the latter towards criticality leaving an anomalously large gap for films where $T_c$ was almost zero [25]. The evolution of both quantities suggests $\Delta$ to survive across the SIT forming a gapped Bose insulator. Similar measurements using planar junctions and disordered 2d InO films [34] compared nominally insulating and superconducting film in the very vicinity of the SIT characterized by dc-transport down to mK temperatures. Surprisingly, both the insulating and superconducting tunneling spectra display a clear gap with almost the same amplitude. The coherence peaks, however, only appear for the latter which was viewed as evidence for robust pairing without global phase coherence in agreement with the bosonic models. In a subsequent publication [35] the insulating gap was conceptually explained by partial screening of electronic interactions due to the nearby metallic tunneling electrode pushing the sample back on the superconducting side to explain an alleged mismatch with optical THz measurements. This argument, however, is questioned by a screening length much smaller than the tunneling barrier. Furthermore, if the electrode effectively pushes an insulating sample superconducting, also the coherence peaks should reappear what is, however, not the case.[49]. Another consequence of strong phase fluctuations manifests at the transition to the normal state. Tunneling studies [36, 31] revealed a pseudogap in the density of states surviving up to several times $T_c$. The gap, however, is not flanked by coherence peaks reminiscent of the superconducting gap. Their absence is understood as result of the vanishing superconducting order, while pair correlations remain present. In this sense, upon cooling preformed Cooper pairs exist at temperatures much higher than $T_c$ but form a globally coherent condensate only below $T_c$. While soon after this discovery, the analogy to the pseudogap in unconventional high-temperature superconductors such as

[47] which can be thought of the energy to be paid for hopping from puddle to puddle.

[48] which is a measure for the energy pay off due to hopping.

[49] The apparent discrepancies between the outcome of optical and tunneling measurements is central part of this thesis and comprehensively discussed in remainder of this chapter.

the cuprates has been stressed, the comparison is delicate as the driving forces - disorder and correlation - are not quite the same. For instance, a recent study [37] assembles experimental evidence that the pseudogap in various cuprates is not restricted to the regime of the phase diagram where phase fluctuations delimit superconductivity (e.g. LSCO) but also appears (in case of e.g. Bi-2201) above amplitude-driven transitions[50]. Although tunneling studies arguably yielded the most valuable insights how energy scales behave towards criticality, the above mentioned discrepancy with optical measurements in the THz frequency range is troubling. The situation is even more alarming as also systematic studies [39, 40] bringing together resonant microwave and tunneling measurements on disordered TiN and NbTiN point towards the insufficiency of theories purely relying on the effects of pair-breaking. In what follows, we present comprehensive measurements of the dynamical conductivity at THz frequencies and compare them to tunneling measurements and discuss a reasonable solution to the above problem on basis of a new kind of excitation invisible to tunneling spectroscopy.

[50] This paradigmatic view of the $T_c-$dome in unconventional superconductors emerging from an amplitude-phase crossover suggested by Emery and Kivelson [38] is, however, challenged by the overwhelmingly complex superconductivity in these compounds.

## 2.3 Measurements of the dynamical conductivity

We now turn to the optical spectroscopy measurements performed on superconducting NbN thin films in appraoch of the SIT. We performed comprehensive measurements of the complex transmission amplitude in the frequency range $\nu = 2-40\,\mathrm{cm}^{-1}$ (i.e. energies $E = h\nu = 0.25-5\,\mathrm{meV}$), which is well suited to study the dynamics of (strong-coupling) superconducting NbN films[51] with critical temperatures ranging between $T_c = 15-3\,\mathrm{K}$ and an estimated spectral gap of $4.2k_BT_c = 0.9-5.4\,\mathrm{meV}$. Measurements were performed in the normal state slightly above $T_c$ and the regime of superconducting fluctuations and in the superconducting states well below $T_c/2$, where the mean-field BCS energy gap is at almost 100% of its zero-temperature value. The spectra of the transmission amplitude and phase were fitted to Fresnel equations via real and imaginary parts of the complex dielectric function $\hat{\epsilon}$ without any particular microscopic model for the

[51] Information on sample growth and -characteristics are found in Sec. A.1.1

charge dynamics[52]. The complex dynamical conductivity follows directly via $\hat{\sigma} = 2\pi i \epsilon_0 \nu(\hat{\epsilon} - 1)$. Prior to the optical studies, similar NbN films with a thickness of 50nm have been fabricated as planar Ag/NbN tunneling junctions. Comprehensive measurements of the (differential) tunneling conductance have been performed by M. Chand and the tunneling spectra displayed below are originally published in Ref. [41].

[52] See Sec. A.3 for more details of this so-called single-peak analysis.

Before we discuss the experimental results, it is instructive to clarify, how superconducting energy scales manifest in both the optical properties and the tunneling conductance $G$. At zero temperature, the charge current $I$ between the electrodes through the tunneling barrier sets in as soon as the Fermi level of the Ag electrode is biased by a voltage $|V| \geq \Delta/e$. As a consequence of the diverging density of states right at $\pm\Delta$, the slope of the conductance $G = I/V$ is initially infinite before it saturates to the tunneling barriers inverse Ohmic resistance. The density of states which is proportional to the differential conductance $\mathrm{d}I/\mathrm{d}V$ displays a gap of the width $2\Delta$ and thus provides a clean access to the superconducting pairing energy. While here, the amplitude of $\Delta$ is measured by shifting chemical potentials, in optical spectroscopy it is probed by the quasiparticle excitations across the gap: At zero temperature, the finite-frequency response of a superconductor sets in at $\nu = 2\Delta/h$ where quasiparticles are lifted above the DOS gap which manifests as an onset in the real part of the dynamical conductivity $\hat{\sigma}(\nu) = \sigma_1(\nu) + \mathrm{i}\sigma_2(\nu)$. While in the canonical BCS picture the onset of electromagnetic absorption at the *spectral* gap $\Omega$ equals the superconducting energy gap $2\Delta$ picture, additional excitations[53] may open absorption channels at frequencies $\nu < 2\Delta/h$ shifting $\Omega$ below $2\Delta$. Consequently, the combination of both transport and optical spectroscopic techniques is a promising route to identify excitations of the superfluid beyond ordinary quasiparticle breaking.

[53] provided that the excitation process is a scalar susceptibility and couples to $\hat{\sigma}$ linearly.

The comparison is done according to the scheme described below.

1. Match an optical with a tunneling spectrum for NbN with (approximately[54]) the identical $T_c$
2. Fit the $dI/dV$ spectrum:
   (a) Solve the Usadel equation (1.48) for a given pair breaking parameter $\tau$ (with $\xi = 0$) and coupling[55] $c = 2\Delta/k_B T_c$ for energies $|E| \geq E_g$ where
   $$\frac{E_g}{\Delta(T)} = \left[1 - \left(\frac{1}{\tau\Delta(T)}\right)^{2/3}\right]^{3/2} \tag{2.10}$$
   is the renormalized hard band gap [8] and $T$ is the temperature of the tunneling measurement.
   (b) Calculate the real part of the energy dependent normal Green function $G(E)$, i.e. the density of states $\mathcal{D}(E)$ via Eq. (1.46).
   (c) Include - if required - additional sub-gap states $N_{\text{tail}}(E)$
   $$\mathcal{D}_{\text{tail}}(E) = \exp\left[\left(\frac{E_g - E}{\Gamma}\right)^{5/4}\right] \tag{2.11}$$
   for $|E| < E_g$ where $\Gamma$ measures the width of the tail accounting for local $\Delta$ inhomogeneities due to random impurity configurations [11].
   (d) Connect $\mathcal{D}(|E| \geq E_g)$ and $\mathcal{D}_{\text{tail}}(E < E_g)$ smoothly by adjusting the relative weight to generate a continuous function $\tilde{\mathcal{D}}(E)$, $\forall E$
   (e) Calculate the functional form of $dI/dV$ at finite temperatures by convoluting $\tilde{\mathcal{D}}(E)$ with the Fermi function $f(E,T)$
   $$\frac{dI}{dV} \propto \frac{d}{dV}\int_{-\infty}^{\infty} dE\tilde{\mathcal{D}}(E)\big(f(E+eV) - f(E)\big) \tag{2.12}$$
   where the integration range is chosen such, that the result does not change any more within standard numerical precision [43]

[54] Any NbN film produced as electrode within a tunneling junction cannot be used for an optical measurement. The relation between the structural properties and the $T_c$, i.e. the reproducibility, is sufficiently high for the given growth procedure, such that the comparison of two NbN films linked by $T_c$ is justified [42]

[55] The temperature dependence of $\Delta$ is assumed to be of BCS type

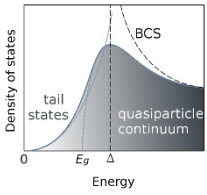


Figure 2.3: Sketch of the disorder-smeared density of states including sub-gap tail states. The dashed line is the BCS solution. Note that the tail states are actually much less significant than displayed here.

(f) Adjust $\tau, c$, and $\Gamma$ and iterate (a-e) to find the optimal fit.

3. Use the obtained $\tau$ and $c$ to solve the Usadel equation for $\Delta(T')$ with $T'$ the temperature of the optical measurement.

4. Calculate the complex normal and anomalous Green's functions $G(E)$ and $F(E)$ via Eqs. (1.46,1.47)

5. Calculate the complex conductivity $\hat{\sigma}(\nu)$ via Eq. (1.52)

Within the canonical BCS picture, the parameters required to fit the tunneling measurement should also yield a proper description of the optical measurement[56].

Figure 2.4 compares measurements of the real part of the dynamical conductivity $\sigma_1(\nu) + \mathrm{i}\sigma_2(\nu)$ of a sample with $T_c = 15.14\,\mathrm{K}$ with a measurement of the differential tunneling conductance $dI/dV$ of a sample with $T_c = 15.6\,\mathrm{K}$. While the tunneling measurement is performed at 1.9 K well below $T_c$, the displayed $\sigma_1(\nu)$ spectrum is taken at 12 K much closer to $T_c$. The reason is that the fully opened gap is located at frequencies above the experimentally accessible range, while the elevated

[56] At the writing of this thesis, we are not aware of a theory for the electromagnetic response including the tail states $N_{\mathrm{tail}}$. Compared to Re$G$, however, the contribution of $N_{\mathrm{tail}}$ to the overall den sity of states is very small here so that negligence thereof will not affect $\hat{\sigma}(\nu)$ substantially.

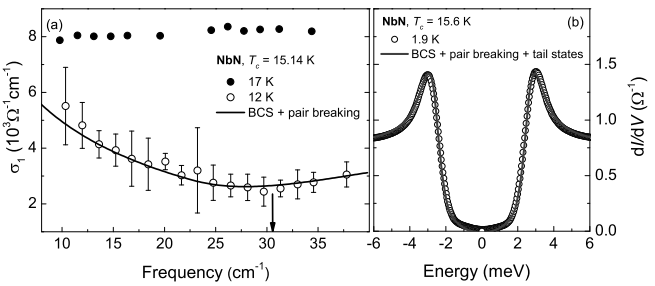


*Figure 2.4:* ***Optical and tunneling spectroscopy on clean NbN.*** *(a) real part $\sigma_1(\nu)$ of the dynamical conductivity in the normal (17 K) and superconducting states (12 K). The arrow indicates the spectral gap estimated from the minimum of $\sigma_1(\nu)$. (b) Differential tunneling conductance $dI/dV$ as function energy at 1.9 K. Solid lines are based on Green's functions calculated for the same pair breaking $\tau$ and ratio $\Delta/k_BT_c$. To fit the in-gap part of $dI/dV$, exponentially decaying tail states have been added, which are not taken into account for $\sigma_1$.*

temperature allows a direct read-out of $\Omega$ and hence comparison with $2\Delta$ from the tunneling measurement. Though being in the clean limit, the coherence peaks in the $dI/dV$ spectrum are smeared out substantially beyond thermal broadening. The optimal fit is obtained for $\tau\Delta_0 = 25.3$ and a coupling of $c = 2\Delta_0/k_BT_c = 4.15$ and a minor $N_{\rm tail}$ contribution. The corresponding prediction for $\sigma_1(\nu)$ invoking the same $\tau$ and $c$ is in very good agreement with the actual experimental result. The minimum in $\sigma_1(\nu)$ lies at $\sim 31\,{\rm cm}^{-1}$ (denoted with the arrow) which gives a coupling $2\Delta_0/k_BT_c = 4.1$ with the BCS temperature-dependence of $\Delta$ [41]. A similar result is found for another pair of clean-limit samples with $T_c = 14.3\,{\rm K}$ and $14.9\,{\rm K}$ for the optical and tunneling measurement, respectively, shown in Fig. 2.5. The minimum in the predicted $\sigma_1(\nu)$ curve is in good agreement with the onset of optical absorption beyond quasi particle dynamics. At sub-gap frequencies, the experimental dispersion matches the predicted one, while above the spectral gap, the rise is stronger than expected. Comparing samples with $T_c = 10\,{\rm K}$ and $9.5\,{\rm K}$ for the optical and tunneling measurement, respectively, reveals an absorption threshold $\Omega$ that is shifted below the predicted one exceeding the range of experimental uncertainty, see the top panel of Fig. 2.6. While again for sub-gap frequencies

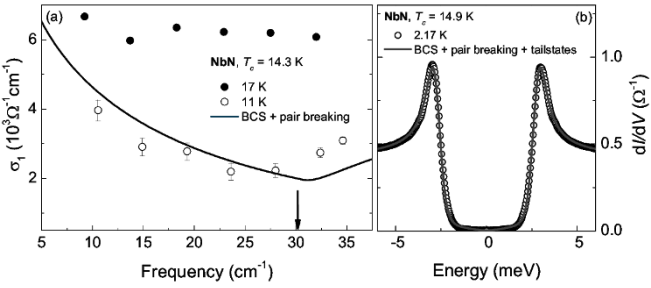


*Figure 2.5:* ***Optical and tunneling spectroscopy on clean NbN.*** *(a) real part $\sigma_1(\nu)$ of the dynamical conductivity in the normal (17 K) and superconducting state (11 K). The arrow indicates the spectral gap estimated from the minimum of $\sigma_1(\nu)$. (b) Differential tunneling conductance $dI/dV$ as function energy at 2.17 K. Solid lines are based on Green functions calculated for the same pair breaking $\tau$ and ratio $\Delta/k_BT_c$.*

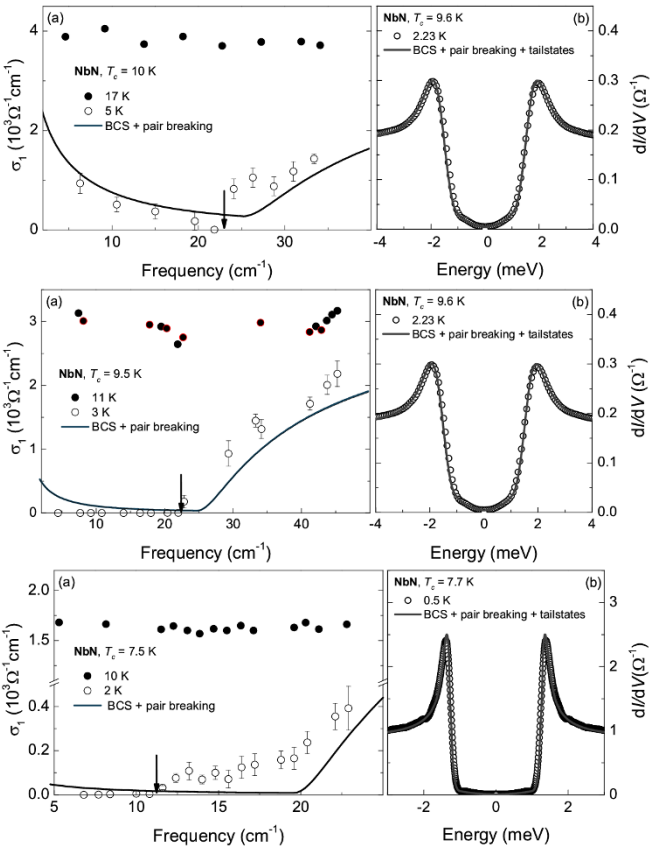


*Figure 2.6:* ***Optical and tunneling spectroscopy on moderately disordered NbN.*** *Panels (a) show real part $\sigma_1(\nu)$ of the dynamical conductivity in the normal and superconducting state. The arrows indicate the spectral gap estimated from the kink of $\sigma_1(\nu)$. Panels (b) display the differential tunneling conductance $dI/dV$ as function energy. Solid lines are based on Green functions calculated for the same pair breaking $\tau$ and ratio $\Delta/k_BT_c$.*

the experimental dispersion agrees with the predicted form, an increasing excess absorption evolves around $\Omega$ and at higher frequencies.

Both the suppression of $\Omega$ with respect to $2\Delta$ predicted from the tunneling measurement and the accumulation of additional spectral weight beyond the quasi-

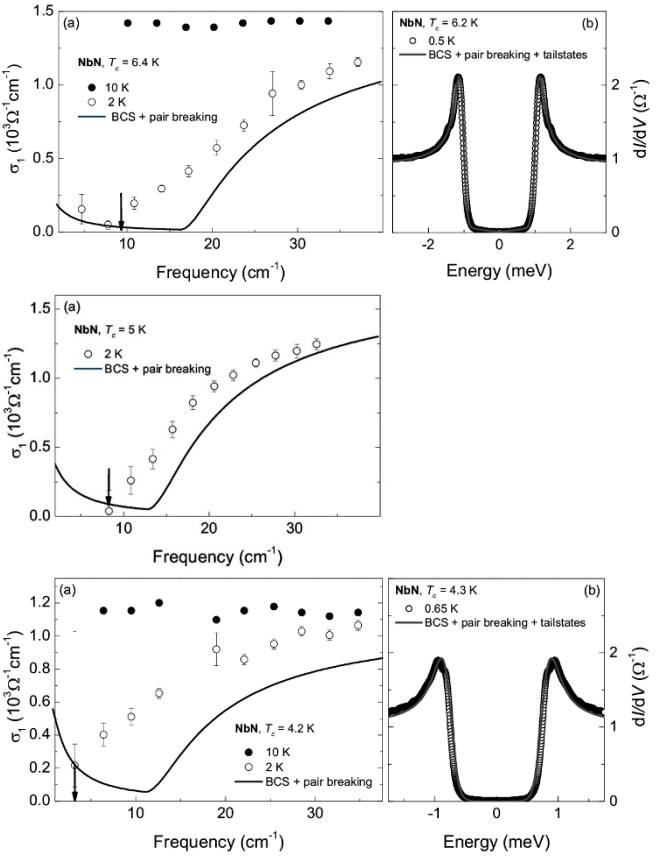


*Figure 2.7:* ***Optical and tunneling spectroscopy on disordered NbN.*** *Panels (a) show real part $\sigma_1(\nu)$ of the dynamical conductivity in the normal and superconducting state. The arrows indicate the spectral gap estimated from the kink of $\sigma_1(\nu)$. Panels (b) display the differential tunneling conductance $dI/dV$ as function energy. Solid lines are based on Green functions calculated for the same pair breaking $\tau$ and ratio $\Delta/k_BT_c$.*

particle absorption, become increasingly pronounced as $T_c$ is reduced in approach of the SIT, as displayed in the mid and bottom panels of Fig. 2.6 and Fig. 2.7. Down to $T_c = 7.5\,\mathrm{K}$ the excess conductivity is concentrated around frequencies corresponding to $2\Delta$ and becomes vanishingly small towards the low-frequency limit. As

for the $T_c = 6.4\,\mathrm{K}$, sample, the additional conductivity spans over the entire frequency range. The discrepancy between the anticipated and the actual $\sigma_1(\nu)$ becomes increasingly worse as both functional form and absolute values are concerned when going to the lowest-$T_c$ sample, where $\sigma_1(\nu)$ could meaningfully be calculated.

As mentioned above, the above fits of the $dI/dV$ spectra to quantify the pair breaking strength incorporated exponential sub-gap tail states, which are not included in the Green's functions $G$ and $F$ from which $\sigma_1(\nu)$ was derived. Piecing together a continuous function $\tilde{\mathcal{D}}(E)$ from both the hard-gapped continuum contribution and the tail states to fit $dI/dV$ is associated with a certain degree of freedom as finite temperatures also smear out a hard gap similar as tail states do. Consequently, the lack of tail states in the calculation of $\sigma_1(\nu)$ should carefully be examined in consideration of the presented discrepancy. This can be done by inversion of the above analysis: $\sigma_1(\nu)$ is fitted to find a suited pair breaking strength, which thereupon is used to calculate a prediction for $dI/dV$. In Fig. 2.8(a) we exemplary re-plot the experimental results on the samples with $T_c = 4.2$ and $4.3\,\mathrm{K}$ together with a fit of $\sigma_1(\nu)$. The required pair-breaking is 10 times stronger than in the previous fit of $dI/dV$ displayed in Fig. 2.7(c). Except for the low-

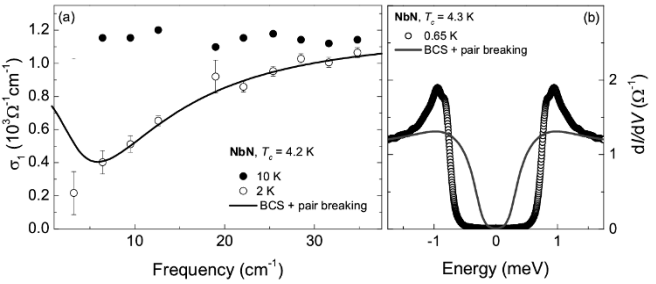


*Figure 2.8:* ***Inverted analysis routine*** *applied to a strongly disordered sample with $T_c$ =4.2 (a) and 4.3 K (b). The pair breaking parameter is chosen such that it yields a fit of $\sigma_1(\nu)$ at 2 K. This strong pair breaking fails to generate a satisfying description of $dI/dV$ regarding both the coherence peaks and the width of the gap.*

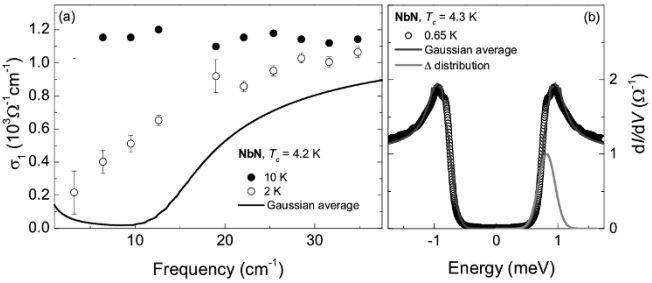


*Figure 2.9:* ***Curves from Gaussian distributed local gaps*** $\Delta(\mathrm{r})$ *applied to a strongly disordered sample with* $T_c = 4.2$ *(a) and 4.3 K (b). The fit of the* $dI/dV$ *measurement is the average of 81* $\mathcal{D}(E)$ *curves calculated from a Gaussian distribution of* $\Delta(\mathrm{r})$ *values. The corresponding average of* $\sigma_1(\nu)$ *curves cannot reproduce the experimental result.*

est frequencies, this choice of pair breaking reproduces the experimental $\sigma_1(\nu)$ very well. At the same time, however, it completely fails to yield a satisfying description of $dI/dV$ displayed in panel (b) regarding both the height and shape of the coherence peaks and the width of the gap. It is clear, that this discrepancy cannot be accounted for by the missing tail states which could only narrow the gap further, and consequently, the effect of tail states on $\sigma_1(\nu)$ can be ruled out as origin of the excess conductivity.

What is the influence of an emergent electronic inhomogeneity? The above $dI/dV$ spectra are measured with planar tunneling junctions. Local tunneling measurements, however, revealed an emergent electronic inhomogeneity on a length scale of the coherence length much greater than the lateral dimension of the planar junctions. In that sense, the smeared $dI/dV$ spectra could also be modeled as an average of locally varying $\Delta(\mathrm{r})$ and thus $\mathcal{D}(E, \mathbf{r})$ curves. In fact, assuming a Gaussian distribution of $\Delta$ values gives a fairly good approximation of the $dI/dV$ spectrum, see Fig. 2.9, although after closer examination it falls short compared to the pair-breaking model. Employing the identical $\Delta(\mathrm{r})$ distribution for an averaged $\sigma_1(\nu)$ curve yields a curve completely at odds with the actual measurement. Attributing the mismatch

between $dI/dV$ and $\sigma_1(\nu)$ measurements can thus not be accounted for by a simple averaged response due to electronic inhomogeneity.

The failure of both pair-breaking and an averaged response due to a distribution of $\Delta(\mathrm{r})$ values as possible underlying scenarios accounting for the apparent mismatch between optical and tunneling spectroscopy calls for an alternative effect at play. In the next section, we will see that three specific properties of NbN - the short coherence length of a few nanometer, the quasi-2d character and the vicinity to quantum criticality - make this material a promising candidate for an excitation best known from the Standard Model of particle physics serving as possible explanation for puzzling observation above.

## 2.4 The Higgs mode and the Higgs mass

The striking resemblance of both the theory of the Higgs boson in high-energy physics and superconductivity gives rise to a natural question: is there a Higgs-boson like excitation in superconductors? Clearly, on the one hand an affirmative answer is challenged by half a century of uncountable spectroscopic measurements *not* revealing a superconducting Higgs mode. On the other hand, the successful and elegant treatment of superconducting phenomena by virtue of field theories and symmetry breaking is a strong pleading for a Higgs mode. Hence, a more constructive approach is not to ask *if* but *where* there is a Higgs mode, and *how* it can be detected experimentally. In recent years, works of Auerbach *et al.* gave a particular clear account to these questions as we will review below.

An instructive way to understand the elusive nature of the Higgs mode is to reconsider under which circumstances the particle analogue appears. The well-defined Higgs boson as sharp resonance is predicted within a *relativistic* and *bosonic* broken-symmetry field theory. Although Cooper pairs as constituents of superconducting condensate can be viewed as composite bosons, the fermionic nature of the underlying quasiparticles usually plays an important role. Qualitatively, this can be

seen as consequence of the pairing taking place in **k**-rather than real space. The coherence length $\xi$, as a measure for the quasiparticle's real-space distance, is for conventional superconductors usually much larger than the inter-atomic distance so that bosonic treatments are not applicable. While Bose-Einstein condensed (BEC) neutral superfluids contain tightly bound pairs and bosonic theories apply, they do not require local $U(1)$ invariance and gauge fields and thus the Higgs mechanism does not occur.

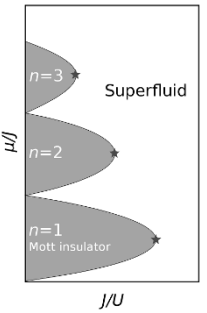


Figure 2.10: Phase diagram of lattice bosons within the Bose-Hubbard model. The tips of the lobes are points with emergent relativistic dynamics. Adopted from Ref. [44].

The search for a suited system with a Higgs mode therefore resorts to effectively bosonic charged superfluids, i.e. short coherence-length superconductors. Thin films of NbN are such candidates: For films of around 50 nm thickness, Hall- and magneto-resistance measurements [45] revealed a coherence length of $\xi \sim 5\,\mathrm{nm}$, which is just around one order of magnitude larger than the lattice constant of NbN and much smaller than the penetration depth $\sim 200\,\mathrm{nm}$ rendering disordered NbN thin-films a prototypical short-coherence superconductor and ideal testbed for effectively bosonic theories.

BEC-like pairs can be treated as lattice bosons within the Bose-Hubbard model (BHM)

$$\mathcal{H} = -J \sum_i (b_i^\dagger b_j + b_j^\dagger b_i) - \mu \sum_i n_i - U \sum_i n_i (n_1 - 1) \tag{2.13}$$

where $b, b^\dagger$, and $n = b^\dagger b$ are bosonic annihilation, creation, and number operators, $J$ and $U$ are hopping and onside-repulsion energies, and $\mu$ is the chemical potential. The phase diagram of this model features insulating and superfluid phases depending on the filling (bosons per lattice site) and the kinetic energy, see Fig. 2.10. By means of a Hubbard-Stratonovich transformation the BHM Hamiltonian can be cast into a field theory with an imaginary-time action reading [46]

$$\mathcal{S}_{BHM} = \int \mathrm{d}\tau \mathrm{d}^d x \mathcal{L}_B \tag{2.14}$$

with the Lagrangian

$$\mathcal{L}_{BHM} = K_0 \psi^\dagger \partial_\tau \psi + K_1 |\partial_\tau \psi|^2 + K_2 |\nabla \psi|^2 + r|\psi|^2 + u|\psi|^4 \tag{2.15}$$

which is identical with the one we discussed in Sec. 1.3.

Clearly, (imaginary) time and space dependencies are not treated on equal footings. It is the linear-time derivative in the first term that spoils relativistic dynamics[57]. In a seminal work [47], however, Fisher et al. have demonstrated that $K_0$ can be related to $r$ via $K_0 = -\frac{\partial r}{\partial \mu}$, and further, that $K_0$ vanishes at the tips of the Mott lobes, see Fig. 2.10. Consequently, the Lagrangian becomes symmetric in space and time coordinates and henceforth describes relativistic bosons. The superfluid-Mott insulator quantum phase transition (QPT) within the BHM has a prototypical condensed-matter realization in form of the superconductor-insulator quantum phase transition (SIT) observed in granular and disordered superconductors such as NbN.

[57] The situation is similar to non-relativistic (Schrödinger) single-particle quantum mechanics

$$(2im\partial_t - \partial_r^2)\psi = 0$$

compared to the relativistic (Dirac) version

$$(i\gamma^\mu \partial_\mu - m)\psi = 0$$

In recent years, the dynamics of the BHM in the relativistic limit have been studied intensively by Auerbach *et al.* in terms of $O(N)$ field theories[58] with an action [49]

$$\mathcal{S}[\phi] = \int \mathrm{d}\tau \mathrm{d}^2x \left\{ \frac{1}{2}(\partial_\mu \phi)^2 + \frac{\mu}{2}|\phi|^2 + g|\phi|^4 \right\} \qquad (2.16)$$

in 2+1 space-time where $\phi$ is an $N-$component real vector. This model has turned out to be a powerful approach to study dynamics and collective modes in quantum critical condensed matter systems, in particular the superfluid-Mott insulator transition [47] for $N = 2$ and Neel-singlet transition of dimerized Heisenberg antiferromagnets [50] for $N = 3$. We will now review some of the results [51, 52, 53, 44] obtained by Auerbach *et al.* relevant for this work.

[58] Note that the description in terms of a the $U(1)$ complex scalar model is here equivalent to the $O(2)$ real vector model [48]

- Relativistic dynamics are essential for the appearance of a long-lived Higgs mode. In the (Gross-Pitaevskii) limit of non-relativistic dynamics, the collective excitations of the order parameter are coupled massless amplitude-phase phonons, whereas for the relativistic case the $O(2)$ model predicts one massless phase mode *and* one massive amplitude (Higgs) mode.

- The aforementioned visibility in the dynamical conductivity does not apply to conventional weak coupling superconductors, where the BCS Hamiltonian commutes with the (Cooper-pair) current op-

erator leaving the spectral gap essentially open. In the strong coupling limit, the coupling between charges and photons happens by gauging the theory as discussed in Sec. 1.3. Via minimal coupling the gauge field $\mathbf{A}$ is introduced and one obtains

$$\mathcal{L}^{O(2)}[\phi, \mathbf{A}] = \frac{1}{2}(\partial_\mu \phi)^2 - \frac{\mu}{2}|\phi|^2 + g|\phi|^4 + \mathcal{L}_{\rm em}[\phi, \mathbf{A}] \tag{2.17}$$

where[59]

$$\mathcal{L}_{\rm em} = e\mathbf{A}(\nabla\pi)\left\{|\langle\phi\rangle_0|^2 + 2\sigma\langle\phi\rangle_0 + ...\right\} \tag{2.18}$$

contains the electron-light interaction. Currents are obtained by functional derivatives of $\mathcal{L}_{\rm em}$ with respect to $\mathbf{A}$. To lowest order, this yields two diagrams: a phase mode $e\nabla\pi$ and a coupled phase-amplitude mode $2e\nabla\pi\sigma$.

- The visibility of the Higgs mode is closely related to the symmetry of the probe. The longitudinal susceptibility of the $O(N)$ field theory in two spatial dimensions diverges at low energies so that the spectral signature of the Higgs mode is washed out into a broad shoulder. However, any scalar susceptibility probing the square of the order parameter rather than its direction, is finite at all frequencies and displays a peak right at the Higgs mass $m_H$ (an energy scale) which manifests as the onset of electromagnetic absorption measured by the dissipative conductivity.

- To understand the physical implications of the above phase-amplitude diagram, we recall the result of Sec. 1.4, i.e. gradients of the superconducting phase, $\nabla\pi$, generate currents and hence cause density fluctuations of the condensate. In 3+1 dimensions, these are massive plasmons with a threshold energy given by plasma frequency $\omega_p$. In turn, while being a sharp resonance in 3+1 dimensions, the Higgs mass $m_H$ is shifted to energies $\hbar\omega_p + m_H$ where the Higgs modes are completely overshadowed by electronic interband excitations and experimental identification is a hopeless task. To the contrary, the plasmons are *not* gapped in 2+1 dimensions due to the nature of Coulomb interaction

[59] Here, we parametrize the order parameter field $\phi$ as

$$\phi = \begin{pmatrix} \langle\phi\rangle_0 + \sigma \\ \pi \end{pmatrix}$$

where $\sigma$ are the longitudinal fluctuations around the ground state $\langle\phi\rangle_0$ and $\pi$ is the phase field. Note, that a real two-component vector is equivalent to a complex scalar order parameter description.

and can be excited at arbitrarily low energies. The excitation threshold for the conductivity is here determined[60] by $m_H$. With $\xi \sim 5$ and $d \sim 20\,\mathrm{nm}$, the NbN films under study are, strictly speaking, not in the actual 2+1 limit, but with $\xi$ and $d$ being of the same order, the dimensional crossover is close such that traces of 2+1 physics are likely to be observed.

[60] Incorporation of higher-order diagrams shows, that the threshold at $\hbar\omega = m_H$ is actually a soft gap closing as $\omega^5$ in leading order suppressed further by a tiny numerical prefactor.

In conclusion, the short-coherence superconductor NbN allows an effective bosonic treatment within the BHM model (and related field theories) and together with the emergent relativistic dynamics in approach of a quantum phase transition is a natural candidate to search for the Higgs mode in a solid-state system. Furthermore, being a scalar susceptibility, the optical conductivity is expected to display an onset of finite $\sigma_1(\nu)$ (for $T = 0$) or a minimum (for $T > 0$) at $m_H$ and therefore is a suited probe for the Higgs mode.

Coming back to the experimental results, we can assemble characteristic features of the $\sigma_1(\nu)$ spectra as function of $T_c$. We start with the energy gap $\Delta$ obtained from tunneling and the spectral gap $\Omega$ being read out from $\sigma_1(\nu)$, see Fig. 2.11. The tunneling gap $\Delta$ is reduced following the strong-coupling BCS prediction indicated by the solid line with $\Delta/k_B T_c = 2.1$ down to the lowest $T_c \approx 3\,\mathrm{K}$. Starting with clean samples far from criticality, corresponding[61] spectral gap $\Omega/2$ also follows the BCS strong-coupling behavior down to $T_c \approx 9\,\mathrm{K}$. Further approach of criticality then pushes $\Omega/2$ below $\Delta$. This relative suppression becomes stronger as $T_c$ goes down. At the lowest-$T_c$ sample[62] the deviation amounts to nearly one order of magnitude. This implies, that while tunneling spectroscopy probes the superconducting energy gap $\Delta$ for all distances from criticality, below a certain $T_c$, another energy scale appears in the optical absorption spectrum. Far from criticality, this additional scale is above $\Delta$, so that $\Omega$ also measures $\Delta$ (or rather $2\Delta$). The reduction below the strong-coupling curve at around 9 K signals the appearance of a new energy scale we interpret as the Higgs mass $m_H$.

[61] Note that the spectral gap for pair excitations lies at $\Omega = 2\Delta$.

[62] Here, $\sigma_1(\nu)$ was measured by means of microwave Corbino spectroscopy. Taken from Ref. [54].

The Higgs mode is a critical mode of the QCP meaning that $m_H$ vanishes as $T_c \to 0$ at the SIT. Within a

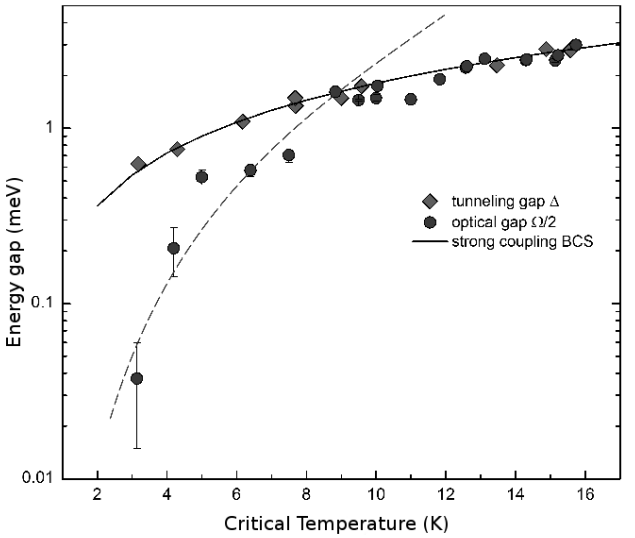


*Figure 2.11:* ***Superconducting energy scales towards criticality*** *Comparison between energy gap $\Delta$ obtained from tunneling measurements and (half of) optical absorption threshold $\Omega/2$ taken as the minimum in $\sigma_1(\nu)$ for NbN films approaching the SIT. In the clean limit (high $T_c$), both energy scales are approximately the same. While the decrease of $\Delta$ follows $T_c$ in agreement with the strong-coupling BCS reduction (black line), the reduction of $\Omega/2$ speeds up towards criticality. The dashed line is a guide to the eye.*

bosonic scenario of the SIT[63], the reduction of $m_H$ below $\Delta$ is a natural consequence, as the pairing energy remains finite across the transition. The increasing reduction of $m_H$ in approach of criticality is in qualitative agreement with the theoretical prediction of the $O(2)$ model, where $m_H \propto (\delta g)^{0.67}$ with $\delta g$ being a dimensionless parameter measuring the distance to the QCP. How $\delta g$ relates to $T_c$ is not a priori clear, so that we can only qualitatively confirm the predicted decay, while affirmation of the exponent remains an open problem.

So far, we have considered only the real part of the complex conductivity. In what follows, we employ the inductive response of the superfluid, $\sigma_2(\nu)$, as a check for internal consistency of the above interpretation.

[63] which seems likely to be realized in NbN, where superconductivity at small order parameters is governed by phase fluctuations [55, 56].

For any system with a constant total carrier density $n_e$, the spectral weight defined as

$$\mathfrak{s} = \int_0^\infty d\omega \sigma_1(\omega) = \frac{\pi n_e e^2}{2m} \tag{2.19}$$

is strictly conserved[64] as it follows from the fundamental Kramers-Kronig relations for causal response functions. The opening of the superconducting gap in $\sigma_1(\nu)$ goes along with a redistribution of spectral weight such that the 'missing' spectral weight at finite frequencies, i.e. the quasi particle contribution $\sigma_{1,QP}$, is compensated by the zero-frequency $\delta$-response, namely the superfluid contribution $\sigma_{1,SF}$, thus

$$\begin{aligned} n_e &= \frac{2m}{\pi e^2} \int_0^\infty d\omega \sigma_{1,n}(\omega) \\ &= \frac{2m}{\pi e^2} \int_0^\infty d\omega \left\{ \frac{e^2 \pi n_s}{m} \delta(\omega) + \sigma_0 \times \sigma_{1,QP}(\omega) \right\} \\ &= n_s + \frac{2m\sigma_0}{\pi e^2} \int_0^\infty d\omega \sigma_{1,QP}(\omega) \end{aligned} \tag{2.20}$$

where $n_s$ is the superfluid density, $\sigma_{1,n}$ the normal-state conductivity, and $\sigma_{1,QP}$ the normalized quasiparticle conductivity scaled with the normal-state dc-conductivity $\sigma_0$. Equation (2.20) holds true for any system where the charge dynamics follows BCS theory. It further states that if $\sigma_0$ is reduced $\sigma_0 \to \alpha\sigma_0$ with $|a| < 1$, then both $n_e$ and $n_s$ are reduced by the same factor $\alpha$. In turn, the appearance of superconducting excitations beyond BCS theory associated with finite-frequency spectral weight calls for a reduction of thereof in a disparate spectral range. For the Higgs mode, being an excitation of the superfluid condensate, a reduction of the superfluid spectral weight is most likely. Indeed, by quantum Monte Carlo (QMC) simulations of the disordered XY-model, Trivedi *et al.* have shown a direct correspondence between the excess spectral weight arising from the Higgs mode and the reduction of the superfluid weight [57].
The superfluid dominates $\sigma_1(\nu \approx 0) \approx \delta(\nu)$ in the zero-frequency limit and therefore, following Kramers-Kronig

[64] Given that the bandmass $m$ also remains constant which in first approximation holds true for non-correlated metals.

relations, also determines $\sigma_2$ at small, but finite frequencies $\nu < 2\Delta/h$. Considering the Kramers-Kronig transform for the superfluid contribution

$$\sigma_2(\omega \approx 0) = -\frac{2}{\pi}\mathrm{P}\int_0^\infty \frac{\mathrm{d}\omega'\omega}{\omega'^2 - \omega^2}\frac{\pi n_s e^2 \delta(\omega')}{2m} \tag{2.21}$$

one finds the relation

$$n_s = \frac{2\pi m}{e^2}\nu\sigma_2(\nu)\Big|_{\nu=0} \tag{2.22}$$

using $\omega = 2\pi\nu$ and $\delta(\omega) = \frac{1}{2\pi}\delta(\nu)$. In practice, we multiply the measured $\sigma_2(\nu)$ with frequency and extrapolate to $\nu \to 0$ to estimate $n_s$. This procedure is comparably reliable as the dependence $\sigma_2(\nu) \propto 1/\nu$ cancels the $n_s \propto \nu$ dependency so that the right side of Eq. (2.22) becomes constant in the low-$\nu$ limit. In Fig. 2.13 we display the product $\sim \nu\sigma_2$ for the NbN films studied in this work. The zero-frequency extrapolation is taken as the mean value of the two left-most data points and shown as star symbols.

To account for the different relative temperatures $T/T_c$ of the various measurements, we correct to thus-obtained value of $n_s(T)$ by assuming the two-fluid approximation [58]

$$\frac{n_s(T)}{n_s(0)} \approx 1 - t^4 \tag{2.23}$$

which only relies on the relative temperature $t = T/Tc$. The applicability of this approximation is shown for a representative sample with $T_c = 6.4\,\mathrm{K}$ in Fig. 2.12(a), where a fit according to Eq. (2.23) yields a satisfying description of the temperature dependence[65].

Figure 2.12(b) compares $n_s(0)$ with the total carrier density $n_e$ obtained by Hall measurements in the normal state [41]. As the resistivity of the films is increased towards criticality, both $T_c$ and $n_e$ are reduced. According to Eq. (2.20) the decline of $n_e$ should cause the same reduction of $n_s$. Experimentally, however, we find $n_s$ to be reduced approximately 10 times stronger than $n_e$ by nearly two orders of magnitude. The progressive suppression of superfluid spectral weight is in agreement with the redistribution thereof at finite frequencies due to the emergence of the Higgs mode. Note that this finding

[65] Note that the zero-temperature extrapolation of $n_s$ and the value at the lowest measurement temperatures differs by less than 5% so that the actual form of $n_s(T)$ plays only a minor role for $n_s(0)$.

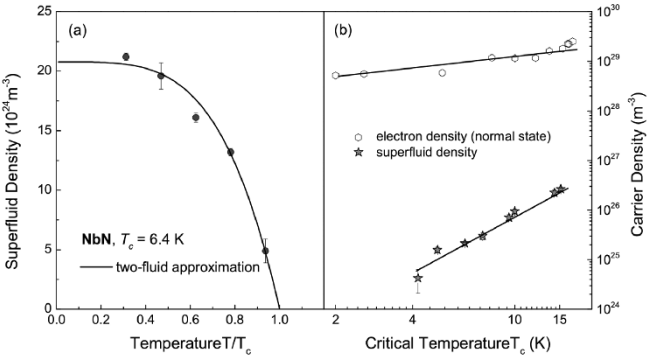


*Figure 2.12:* ***Superfluid and total carrier densities*** *(a) temperature dependence of the superfluid density $n_S$ for a sample with $T_c = 6.4\,K$. The solid line is a fit to the two-fluid approximation giving a zero-temperature extrapolation of $n_s(0) = 2.07 \times 10^{25}\,m^{-3}$. (b) Comparison between the total carrier density $n_e$ [41] from normal-state Hall measurements and the zero-temperature superfluid density obtained from $\sigma_2(\nu)$. Note the stronger decay of $n_s$ compared to $n_e$ in agreement with a redistribution of spectral weight weakening the superfluid contribution towards criticality. Lines are guides to the eye.*

also proves the superconducting origin of the excessive dynamical conductivity in $\sigma_1(\nu)$ and rules out a redistribution of spectral weight from higher energies due to, e.g., a change in the plasma frequency.

Finally, we address the dispersion of the Higgs mode. For this we subtract the predicted $\sigma_1(\nu)$ curves based on the tunneling pair-breaking strength from the actual measurements. The upper panel of Fig. 2.14 displays $\sigma^{\mathrm{Higgs}}(\nu)$ extracted for four samples[66] with $T_c = 7.5 - 4.2\,\mathrm{K}$. Although the studied spectral range allows to capture the major part of the Higgs mode (displayed as thick lines), its connection to the quasi particle curve at high frequencies (thin lines) is not fully recovered for all samples. To calculate the spectral weight of the Higgs mode for a quantitative comparison with the reduction in $n_s$, an extrapolation is required, whose particular form, however, strongly affects the resulting integral. Unfortunately, the inaccessible high-frequency tail renders a quantitative spectral weigh analysis impossible. Never-

[66] Although traces of excessive conductivity appear in samples with $T_c$ up to 14.3 K, a *meaningful* isolation of $\sigma^{\mathrm{Higgs}}$ only works for the samples shown in Fig. 2.14 due to the finite data spacing.

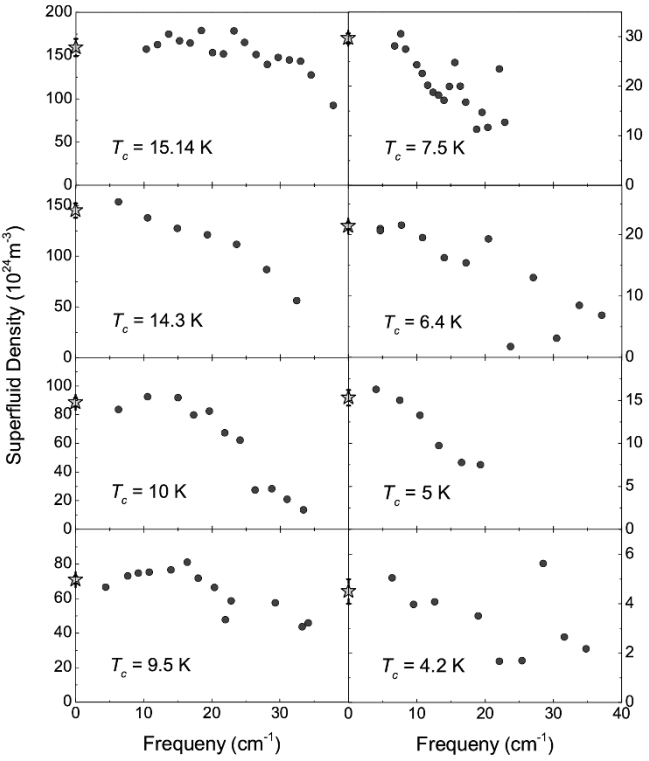


*Figure 2.13:* ***Determination of the superfluid density*** *The figure assembles experimental results on the inductive response of NbN samples under study multiplied with frequency, $\nu\sigma_2$ which according to Eq. (2.22) measures the superfluid density in the limit $\nu \to 0$ (shown as stars)*

theless, some important connections can be made to theory. The lower panel of Fig. 2.14 displays the theoretical prediction of the bare Higgs mode conductivity obtained from Quantum Monte-Carlo studies of the disordered XY Hamiltonian [57] at various distances from the SIT measured in terms of the disorder parameter $p$. To relate the energy scale of the simulation, the Josephson energy $E_J$, to experiment, one can estimate $E_J$ from the clean-sample $T_c$ as $E_J = 2k_BT_c/\pi$ [59] yielding $\sigma^{\rm Higgs}/\sigma_0$ $E_J \approx 0.8\,$meV. In experimental units, the energy scale in the lower panel of Fig. 2.14 would then cover frequencies

$0 - 64\,\mathrm{cm}^{-1}$ similar to the measurement range. Comparing the measured and simulated $\sigma^{\mathrm{Higgs}}$ reveals a fundamental resemblance: starting far from criticality, both amplitude and width of the mode increase towards the SIT. At the same time, a pronounced peak evolves that

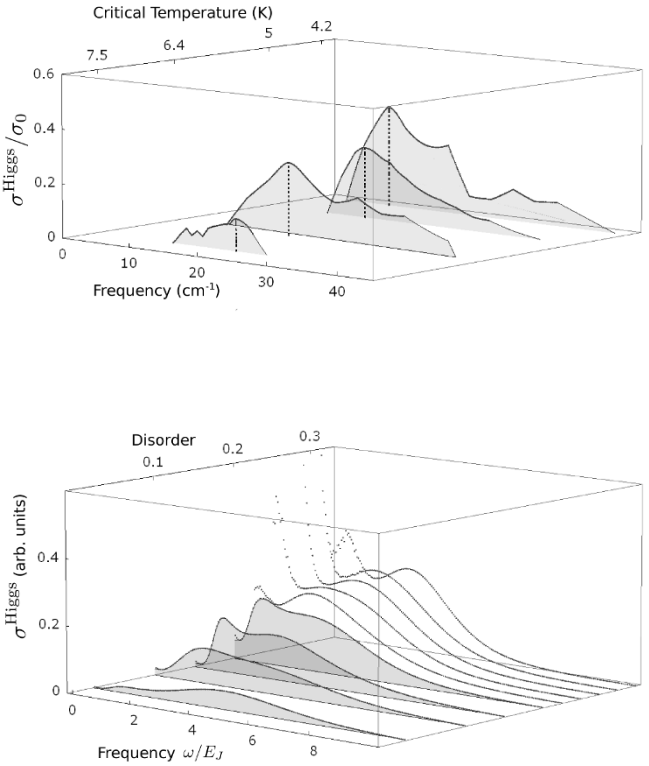


*Figure 2.14:* ***Higgs conductivity in experiment and theory.*** *Top panel: excessive conductivity extracted by subtraction of the quasiparticle contribution from the experimental $\sigma_1(\nu)$ for various films towards criticality. As $T_c$ goes down, the mode grows in spectral weight and acquires a maximum shifting towards lower energies. Bottom panel: Higgs conductivity calculated from QMC simulations of the disordered XY Hamiltonian [57] at various disorder values. Shaded curves are chosen for comparison based on line shape similarities to the experiment.*

grows in amplitude and shifts towards lower energies. A close examination, however, also reveals differences: While the clean onset of absorption at $m_H$ of the $O(2)$ model is somewhat washed out by disorder, the measured $\sigma^{\text{Higgs}}$ displays a clear onset at finite energies. This points towards the important question of the interplay between disorder, the SIT, and the Higgs mode we will address in the next section.

In conclusion, by systematic comparison of tunneling and optical measurements on a set of NbN films tuned towards the SIT we unraveled an energy scale that shifts below the superconducting energy gap $\Delta$ associated with the emergence of an enhanced conductivity at energies around $2\Delta$. Neither disorder enhanced pair-breaking effects nor an inhomogeneous spatial gap distribution could explain the evolution of the additional spectral weight and shift of absorption threshold towards criticality. Instead, we suggest that the vicinity to quantum criticality and the short coherence length of the quasi-2d films allow a treatment within the fully relativistic bosonic $O(2)$ field theory. Within this framework, we interpret the additional absorption channel beyond quasiparticle dynamics as the collective amplitude mode of the superconducting order parameter, namely the Higgs mode, and the new energy scale diving below $\Delta$ as the Higgs mass $m_H$. The appearance of the Higgs mode goes hand in hand with an anomalous reduction of superfluid density and is in good agreement with the line shape predictions obtained from Quantum Monte Carlo simulations of the disordered $XY$ Hamiltonian. The observation of the softening Higgs mode is a direct proof that the SIT is a quantum critical point in which a diverging timescale is detected [60]. Evidently, the vicinity to the QPT offers a unique opportunity to study the nature of the low energy collective excitations in superconductors. As a prototype of quantum criticality, the findings presented here also have implications on broader questions about the effects of interactions and disorder in condensed matter, and to related questions in interacting cold atoms and quantum statistical mechanics.

## 2.5 Some concluding remarks on the Higgs mode in disordered systems

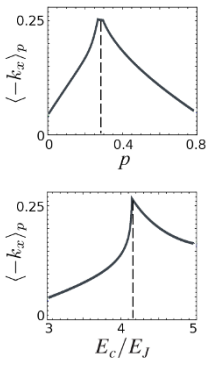


Figure 2.15: Average total kinetic energy obtained from simulations of the XY Hamiltonian as functions of disorder $p$ and the Coulomb-to-Josephson energy ratio $E_C/E_J$. The SIT (dashed lines) can be realized by tuning $p$ or $E_C/E_J$. Adopted from Ref. [57].

In the previous sections we considered NbN films tuned to quantum criticality by increasing disorder. Indeed, disorder certainly increases as measured by the increasing normal state resistivity and, e.g., the Ioffe-Regel parameter $k_F\ell$ [41]. Considering disorder, however, as the underlying mechanism *driving* the thin films from superconducting to insulating phases, may lead to troublesome inconsistencies in the above interpretation that deserve a closer examination. In what follows, we will first argue, that disorder increases, but not necessarily causes the SIT, and, by this, justify the applicability of the disorder-free $O(2)$ field theory on which the above interpretation is essentially build on.

The experimentally detected Higgs modes, displayed in the upper panel of Fig. 2.14, were qualitatively mapped to simulations of the *disordered* $XY$ Hamiltonian. In particular, the highlighted curves in the lower panel of Fig. 2.14 correspond to disorder parameters $p$ =0.025, 0.1, 0.15, and 0.2 which have to be compared to the value at the SIT, $p_c = 0.337$. While the assignment $T_c - p$ was done here considering similarities of experiment and theory, establishing a direct relation between both parameters is delicate. A possible route includes the average kinetic energy along the $x$-bonds in the disordered $XY$ square lattice, $\langle -k_x \rangle$, given as [57]

$$\langle -k_x \rangle_p = \frac{1}{\pi} \int_{-\infty}^{\infty} d\omega \left\{ n_s \delta(\omega) + \sigma^{\text{Higgs}}(\omega, p) \right\} \qquad (2.24)$$

which relates to the experimentally accessible sheet resistances $R_\square$ of clean and disordered systems as [59]

$$\frac{R_\square(\text{disordered})}{R_\square(\text{clean})} = \frac{\langle -k_x \rangle_p}{\langle -k_x \rangle_{p=0}}. \qquad (2.25)$$

The left-sided ratios of Eq. (2.25) for the samples under study are approximately 1.45, 1,5, 1.66, and 2.43 in approach of the SIT. The corresponding $p$-value, see Fig. 2.15 are approximately $p$ =0.029, 0.033, 0.043, and

0.092, i.e. systematically lower than the anticipated values above. This could, on the one hand, suggest that with the critical disorder $p_c = 0.337$, the samples under study are still far from the SIT which appears rather unlikely considering the massive suppression of $T_c$. Alternatively, the SIT in thin films of NbN might not necessarily be driven by disorder, but instead the competition between Coulomb and Josephson energies, i.e. localization and mobility of charges. This second route envisions a SIT even for zero disorder, when the system falls apart into superconducting islands decoupled from each other, so that Cooper pairs are localized. This scenario of an emergent electronic inhomogeneity is supported by local measurements of the order parameter amplitude $\Delta(\mathrm{r})$. In addition, the sharpness of the SIT in NbN favors a transition driven by $E_C/E_J$ instead of pure disorder, which would rather destroy the QCP and turn the direct SIT into a blurred superconductor-metal-insulator transition [48]. Unfortunately, we cannot directly compare our excess conductivity shown in Fig. 2.14 to simulations for a $E_C/E_J$ driven SIT as these data have been made public only in parts. The main difference [57] between the predictions for $\sigma^{\mathrm{Higgs}}$ from the $p$ and $E_C/E_J$ scenarios, however, is a well-defined absorption threshold at the Higgs mass all the way to the SIT in case of the latter in agreement with both our experimental findings and the results of the relativistic $O(2)$ field theory. In the light of these considerations, the SIT in thin films of NbN is likely to be driven by a localization/delocalization mechanism, where Cooper pairs become trapped in emergent superconducting islands towards the QCP. The subordinate role of disorder is important also from another point of view: As discussed previously, the Higgs mode appears from a Lagrangian with relativistic dynamics, i.e. obeying Lorentz invariance. The latter is characterized by a dynamical critical exponent of $z = 1$. For the disordered superfluid-Mott transition in bosonic systems, one finds $z = 1.65$ [61] which consequently spoils relativistic dynamics and existence of a well-defined Higgs mode. In addition, Benfatto *et. al* have shown that once disorder is introduced, the amplitude and phase fluctuations of the order parameters are mixed so that one can no longer speak of separate dispersive amplitude and phase modes [62, 63]. At the same time, the Higgs mode considered

here is a $\mathbf{q} = 0$ mode and so it is not strongly affected by the lattice and lattice disorder. Furthermore, near the clean QCP, the Higgs mode provides the dominant contribution to the spectral weight which cannot suddenly disappear once weak disorder is introduced. At the time of writing this thesis, there is no consensus on the relative importance of amplitude and phase modes in weakly disordered systems. While calculations up to the random-phase-approximation (RPA) level [62, 63] put emphasis on the latter, the more fundamental QMC simulations [57] favor the first[67].

[67] Although only the RPA analysis allows to clearly disentangle phase and amplitude contributions, which is not possible in the QMC simulations.

Finally, we note similar THz time-domain measurements as discussed in this chapter have been conducted by Armitage *et al.* [64] shortly after we had published

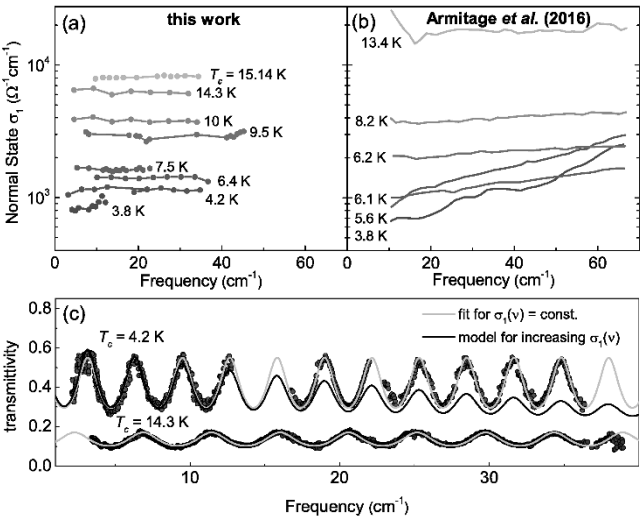


*Figure 2.16:* ***Normal-state optical data*** *for various NbN films measured by (a) frequency domain THz spectroscopy (this work) and (b) time-domain THz spectroscopy (values taken from [64]). While the experimental studies presented in this work reveal a frequency-independent $\sigma_{1,n}$, a growing rise with frequency is reported in Ref. [64]. (c) Raw transmittivity spectra for two films (this work) far and close to the SIT together fitted by a frequency-independent Drude conductivity (light gray) and a curve assuming a dispersion similar to the $T_c = 3.8\,K$ sample of panel (b).*

our main results. While the main experimental finding, i.e. the impossibility to explain the optical results on pure basis of pair-breaking induced from tunneling measurements, is identical with what is presented in detail in Sec. 2.3, the experimental outcomes concerning the normal state conductivity $\sigma_{1,n}(\nu)$ differ significantly: In this work, $\sigma_{1,n}(\nu)$ reveals (within the experimental error bars) a flat Drude response which is seemingly at odds with the results of Ref. [64], where $\sigma_{1,n}(\nu)$ grows with frequency towards criticality, see Fig. 2.16(a,b). The authors of Ref. [64] attribute this to the localization tendencies of the charge carriers and restrict their analysis to the normalized superconducting spectra to meet the requirement for a dispersion less normal state withing the standard BCS expression for $\sigma_1(\nu)$. Such a normalization is not required for the data presented and discussed in this work. To rule out a systematic error stemming from our $\hat{\sigma}(\nu)$ analysis, we can directly compare the raw transmittivity spectra, $\mathcal{T}(\nu)$, of two films far ($T_c = 14.3\,\mathrm{K}$) and close ($T_c = 4.2\,\mathrm{K}$) to the SIT, see Fig. 2.16(c). Irrespective of $T_c$, the $\mathcal{T}(\nu)$ spectra do not feature any frequency dependence beyond the Fabry-Perot pattern in favor of a frequency independent film conductivity, which is supported by a perfect Drude fit with a relaxation rate at eV energies or higher. For comparison, another $\mathcal{T}(\nu)$ curve is shown based on a conductivity rise similar of the $T_c = 3.8\,\mathrm{K}$ sample displayed in Fig. 2.16(b) clearly at odds with our measurement. Although the spectral range of Ref. [64] is greater by a factor of two so that a frequency dependence can more easily be traced, the different results and how they may be related to an technical origin, remain an open problem.

At about the same time the results of this chapter were published, another superconducting excitation also termed *Higgs mode* has been reported by Matsunaga *et al.* by measuring the dynamics of the energy gap $\Delta$ of the BCS superconductor $Nb_{1-x}Ti_xN$ in the non adiabatic regime after an intense THz pulse [65]. These studies revealed an oscillatory behavior of $\Delta(t)$ quickly leveling off to the equilibrium value $\Delta_0$, which can be understood using the BCS Hamiltonian expressed in terms of pseudo-spins introduced by Anderson. This *Higgs*

*mode*, however, is qualitatively distinct from the relativistic *Higgs mode* of the $O(N)$ field theory. While the mode reported in Ref. [65] resides exactly at $2\Delta$ and is a consequence of the single-particle DOS of weak-coupling BCS superconductors[68], the quantum-critical mode presented in this work is a strong-coupling mode with an energy solely determined by the distance to the QCP not related to $\Delta$ at all [48]. The question, which of both modes should meaningfully be interpreted as the Higgs particle analogue, is not only of semantic nature. The Higgs particle is a bosonic excitation of longitudinal components of the Higgs field which obeys relativistic dynamics. The strong-coupling Higgs mode emerges from the essentially identical Lagrangian with no fermionic degrees of freedom and becomes well-defined only below $2\Delta$ towards criticality. Here, the composite nature of Cooper pairs and the superconducting scale $\Delta$ becomes irrelevant, which is clearly not the case for the weak-coupling mode residing exactly at $2\Delta$. Furthermore, the strong-coupling mode follows from the $O(N)$ model as an excitation of the order parameter field $\psi$, while the weak-coupling mode is an oscillation of the energy gap $\Delta$, which, strictly speaking, is not the same[69]. In that sense, linking the strong coupling mode to the Higgs particle is not only reasonable, but also allows a fascinating view on the universe: When crossing from insulator to superconductor within the $O(N)$ model, the ground state of the symmetric order-parameter field $\psi$ starts with an expectation value of $\langle\psi\rangle_0 = 0$ and there is no Higgs mode, while in the superconducting broken-symmetry phase $\langle\psi\rangle_0 \neq 0$ and a Higgs mode emerges. In the identical sense, the universe passed through a critical point shortly after the Big Bang, when the temperature dropped below the electroweak unification scale of about 250 GeV. Today, the ground state of the Higgs field breaks symmetry giving rise to massive Higgs bosons, which are - so to speak - nothing else but critical modes of the early-universe phase transition.

[68] Pictorially, the weak-coupling mode can be understood as a coherent *breathing mode* of Cooper pairs oscillating around their center of mass [66].

[69] In fact, using $\Delta$ as the superconducting order parameter is a reasonable approximation for BCS superconductors, which, however, may break down in presence of strong pair-breaking as shown early after BCS by Abrikosov and Gor'kov, when the energy gap vanishes, while superconductivity persists [20, 21, 22].

http://www.springer.com/978-3-319-72801-8

Electrodynamics of Quantum-Critical Conductors and Superconductors

Pracht, U.S.

2018, XX, 176 p. 62 illus., 1 illus. in color., Hardcover
ISBN: 978-3-319-72801-8